PROCEEDINGS, 51st Workshop on Geothermal Reservoir Engineering
Stanford University, Stanford, California, February 9-11, 2026
SGP-TR-230

Evidence of Direct Fluid Connections between Hydraulic Fractures and Pre-existing Faults at the Cape Station EGS Project

Taeho Kim[1], Eric M. Dunham[2], Sireesh Dadi[3], Paul Segall[2], Richard L. Gibson Jr.[3], Aleksei Titov[3], Shanna Chu[3], Jack Norbeck[3]

[1]Department of Energy Science & Engineering, Stanford University

[2]Department of Geophysics, Stanford University

[3]Fervo Energy

Corresponding author: kimtaeho@stanford.edu

Keywords: Enhanced Geothermal Systems, Hydraulic fracturing, Induced seismicity, Physics-based modeling

ABSTRACT

We present unique observations and models of hydraulic fracture-fault interactions from the Cape Station EGS project operated by Fervo Energy. We focus on the multi-stage, plug-n-perf stimulation of three horizontal wells near a vertical monitoring well that hosts a downhole pressure gauge. Faults were identified by clustering the microseismicity catalog through unsupervised clustering algorithms. We focus on a fault that intersects multiple horizontal wells and passes closely to the pressure gauge. The initial shear to effective normal stress ratio on the fault is between 0.31 and 0.45; approximately 7 – 18 MPa pressure increase is required to reach criticality for a friction coefficient of 0.6. The pressure gauge recorded two increases of approximately 20 MPa each, interpreted as follows. The first increase occurred during stimulation of the first well and is consistent with fluid leak-off and pressure diffusion away from a nearby hydraulic fracture into the low permeability reservoir. This pressurization of the reservoir brought the fault to a critically stressed state. The leak-off model cannot explain the second, more rapid and larger pressure increase observed during stimulation of the two additional wells, which is more consistent with pressure transmission along a high-permeability fault zone. Seismicity initiated near, but some distance away from where hydraulic fractures intersect the fault. The lack of seismicity close to a minor casing deformation implies that slip occurred aseismically in these regions. We test the hypothesis of pressure transmission along a high permeability fault zone using 3D modeling of fault zone fluid transport. The strong correlations between fault slip, fluid pressure, and well deformation highlight the crucial impact that fault structure and adjacent, permeable damage zones can have on stimulation. Our study demonstrates the importance of pre-existing faults and the potential value of physics-based modeling, integrated with geophysical and geomechanical data, in managing EGS stimulations.

1. INTRODUCTION

Next-generation technologies in geothermal energy that target deep, low-permeability rock formations face high chances of encountering faults. Faults can provide high permeability pathways to flow along the fault and/or act as barriers to across-fault flow. Changes in pore pressure and poroelastic stresses can activate fault slip, either seismically or aseismically. In some notable cases, induced seismicity has terminated operations entirely (Häring et al., 2008, Kim et al., 2018). Fault slip can dynamically increase fault zone permeability (Cappa et al., 2022a, 2022b, Guglielmi et al., 2015). This has the potential for increasing the surface area available for heat exchange, provided that the faults are not so permeable that they hydraulically short-circuit the reservoir between wells. Scaling up geothermal energy requires informed management of hydraulic stimulation operations of faulted reservoirs, with the dynamic interplay between fluid injections, pressure diffusion, and fault slip being a fundamental part of reservoir engineering.

This study presents the findings from detailed analysis and modeling of fracture-fault interactions during recent stimulations by Fervo energy at Project Cape. The multi-stage, plug-n-perf stimulation of three horizontal wells triggered seismicity and induced significant increases in the pressure at a downhole pressure gauge. Our analysis of these observations, through 3D coupled modeling of hydraulic fractures and along-fault pressure diffusion, demonstrates the existence of a high permeability fault zone that makes direct connections to hydraulic fractures. The following sections describe in greater detail our reasoning and methodology.

2. OVERVIEW OF THE STIMULATION AND RESULTANT FAULT ACTIVATION

We focus on operations around the Frisco pad in the southern portion of Project Cape. The Frisco pad has three horizontal wells (3-I, 2-P, and 1-I, from south to north) that were stimulated and one open-hole well (4-T, north of the other wells) that was unstimulated. Nearby is a vertical monitoring well (Delano). The Delano well was equipped with a downhole pressure gauge at the depth of stimulation and an optical fiber to measure strain rate. Figure 1 shows the map and depth-section views of the well positions along with the local geology and estimated isotherms.

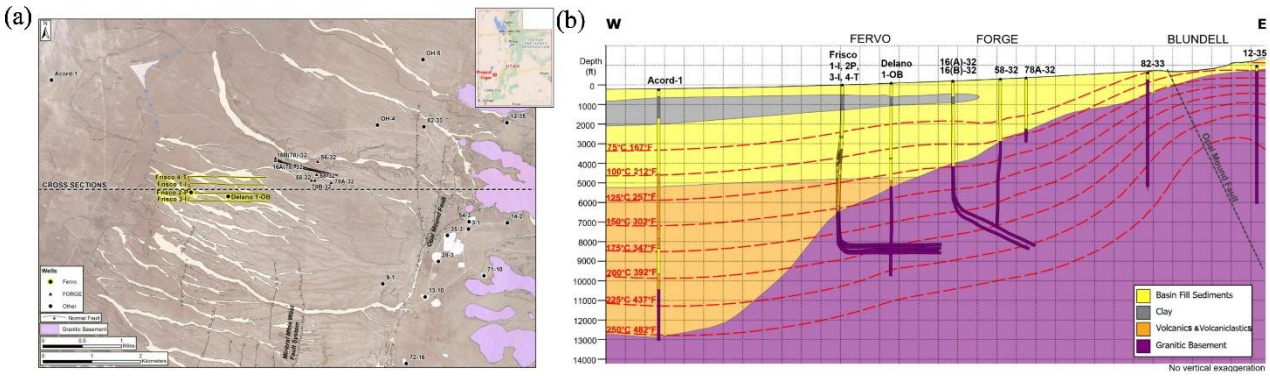

Figure 1: (a) Map view of the Frisco pad (highlighted in yellow) at Cape station, Utah, in close proximity to Utah FORGE situated more northeast (figure from Fercho et al., 2024). (b) Depth-section view of the Frisco pad, indicating that injections happen in a granitic basement around the depth of 8,500 ft from the surface (figure from Fercho et al., 2024).

The chronology of the stimulation is as follows: The 1-I well was first stimulated in its entirety. Then, the first 10 stages of the 3-I were stimulated after which a zipper-fracking sequence began between wells 3-I and 2-P. The wireline deployment of the plug and perf gun for the stimulation of stage 3 along well 2-P was blocked by a casing deformation (Figure 2) that prevented further stimulation during the time period that we study. Later, the remaining stages of 2-P were successfully stimulated by using a smaller inner diameter plug. In the meantime, the remaining stages of 3-I were stimulated. We focus mainly on the stimulations of 3-I and 1-I, and in particular the stages that likely propagated hydraulic fractures that grew closest to the Delano pressure gauge. Stimulation of the first two stages of 2-P, close to the toe of that well, are neglected as they likely have little to no impact on our analysis, due to their large distances from the Delano pressure gauge.

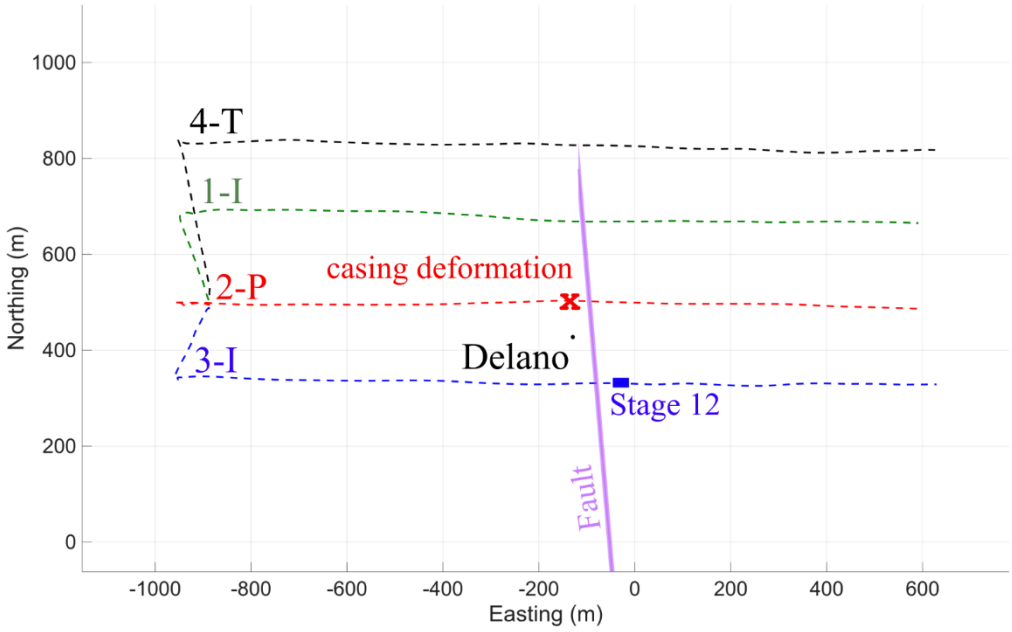

Figure 2: Well trajectories in map view. The shaded purple line shows a cross-section of the fault identified near the Delano pressure gauge at the depth of stimulation.

2.1 Fault Identification and Assessment of Initial Conditions and Aseismic Slip

The relocated catalog of the microseismicity that was recorded during all stimulations (1-I, 2-P & 3-I) and the circulation tests that followed is shown in Figure 3. Multiple faults are evident in the microseismic event catalog (Fig. 3a). Our modeling efforts are focused on one fault (Fig. 3b) that we identified using a four-step clustering algorithm: 1) initial clustering with HDBSCAN (Hierarchical Density-Based Spatial Clustering of Applications with Noise), 2) agglomerative merging based on co-planarity, 3) drawing of best fitting planes by PCA, and 4) density-weighed assignment of events to nearest planes. The fault passes closely to the Delano pressure gauge (Figure 2), providing unique constraints on the processes that led to fault activation.

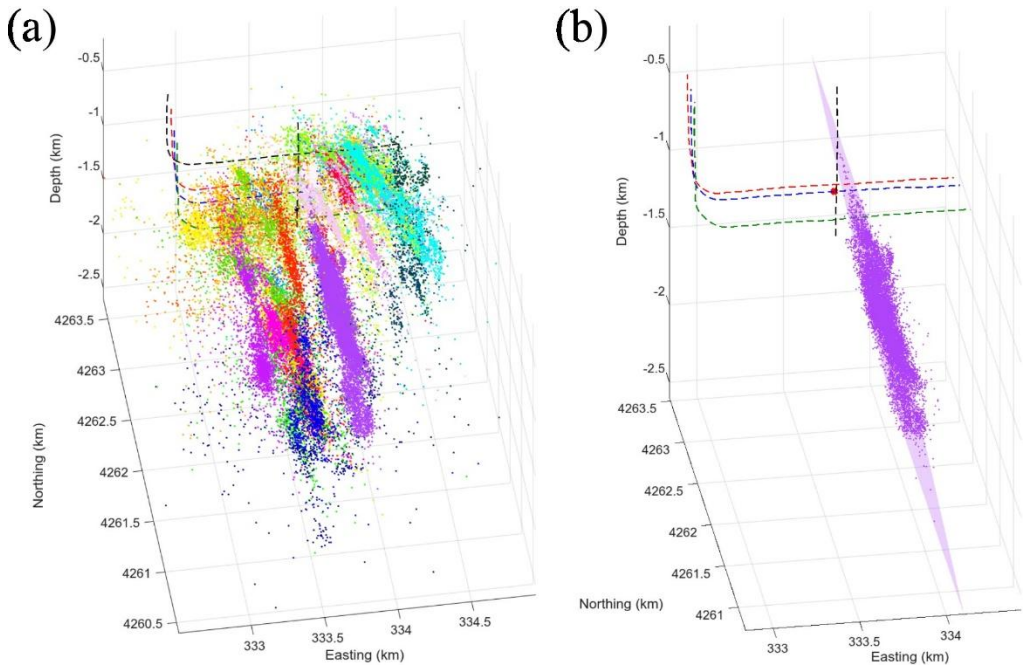

Figure 3: (a) Relocated catalog of the microseismicity from all stimulations and circulation tests. The colors represent individual clusters that were identified to distinguish events between different faults. (b) We single out the fault most likely to have caused the casing deformation along 2-P (red dot) and the pressure increases at the Delano gauge given its spatial proximity and the timing of microseismic activity.

The proximity of the intersection between the fault and the 2-P well to the casing deformation (Figure 3) makes slip on this fault the most likely cause. We project the seismic slip of all earthquakes associated with the fault that were triggered onto the best fitting fault plane, assuming a circular crack with a constant 3 MPa stress drop (Figure 4). There is little to no seismic slip around the intersection between the fault and the 2-P well, indicating that aseismic slip, undetected by seismic monitoring, caused the casing deformation.

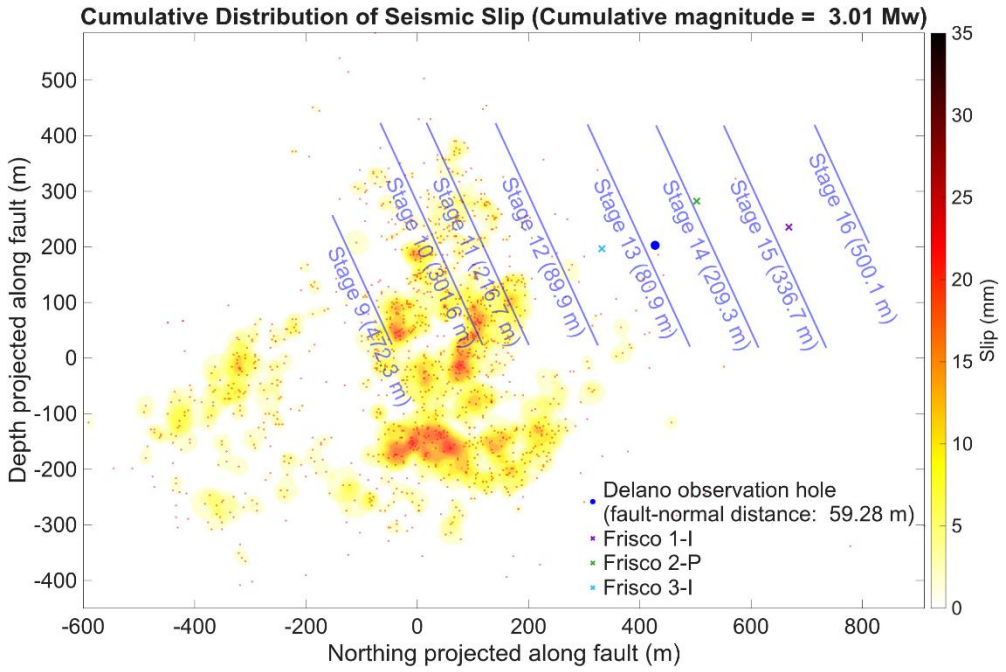

Figure 4: Cumulative distribution of seismic slip from all earthquakes associated with the fault identified in Figure 3b that were triggered. The blue dot shows the location of the Delano pressure gauge projected onto the fault with a fault-normal distance of about 60 m. The x's indicate locations where wells cross the fault. The blue lines show potential intersections between the fault and hydraulic fractures from 3-I with the distance in parentheses indicating the along-fracture distance to the fault from the injection points. The hydraulic fractures will not intersect the fault if their half-length is less than this

distance. Note the lack of seismic slip around the intersection with the 2-P well. This shows that aseismic slip caused the casing deformation.

We used constraints on the orientation of the maximum principal stress (about 15° East of North) from borehole breakouts (Fercho et al., 2025), initial pore pressure, and vertical total stress from density logs to resolve the shear stress and effective normal stress on the fault prior to stimulation. This problem is underdetermined and requires an additional constraint. We explored two possibilities. In the first approach, we used an estimate of the ratio R of the three principal stresses from focal mechanisms (Mohammadi et al., 2025). The dominant focal mechanism near the fault is strike-slip, giving an R value of 0.5. In the second, we assumed a critically stressed crust (with a friction coefficient of 0.6, representative of granite). We found that the initial shear to effective normal stress ratio on the fault is between 0.31 and 0.45, and approximately 7 – 18 MPa pressure increase is required to reach criticality (Figure 5). This means that the fault was far from failure initially and therefore probably long dormant.

3. MODELS OF DOWNHOLE GAUGE PRESSURE

Fig. 5 shows the surface treating pressure during stimulation of 1-I and 3-I along with the Delano downhole gauge pressure. There are two notable pressure increases on the Delano gauge. The first occurs during the initial 1-I stimulation following stage 13. The pressure begins to increase after shut-in, prior to the subsequent stimulation of stage 14. Pressure continues to build up throughout subsequent stages until stage 17, after which pressure starts to decay. The peak pressure increase is sufficiently large (~20 MPa) to bring the fault to failure. However, minimal seismicity occurred on the fault at this time. The rate of pressure decay decreases until the next pressure increase begins during the stimulation of stage 8 along 3-I (Figure 5). Pressure increases dramatically during the stimulation of stage 12 on 3-I, before decaying rapidly after shut-in. This cyclic pressurization-depressurization response continues for stages 13-16, giving multiple spikes in the pressure recording. We attribute the pressure increase during the stimulation of 1-I to leak-off from hydraulic fractures that pass within a few meters of the Delano gauge. The multiple pressure spikes during the stimulation of 3-I are explained by fluid injection through hydraulic fractures into a fault damage zone that has high permeability, at least in the region between the hydraulic fracture-fault intersections and the Delano gauge. The following subsections explain the analyses in greater detail.

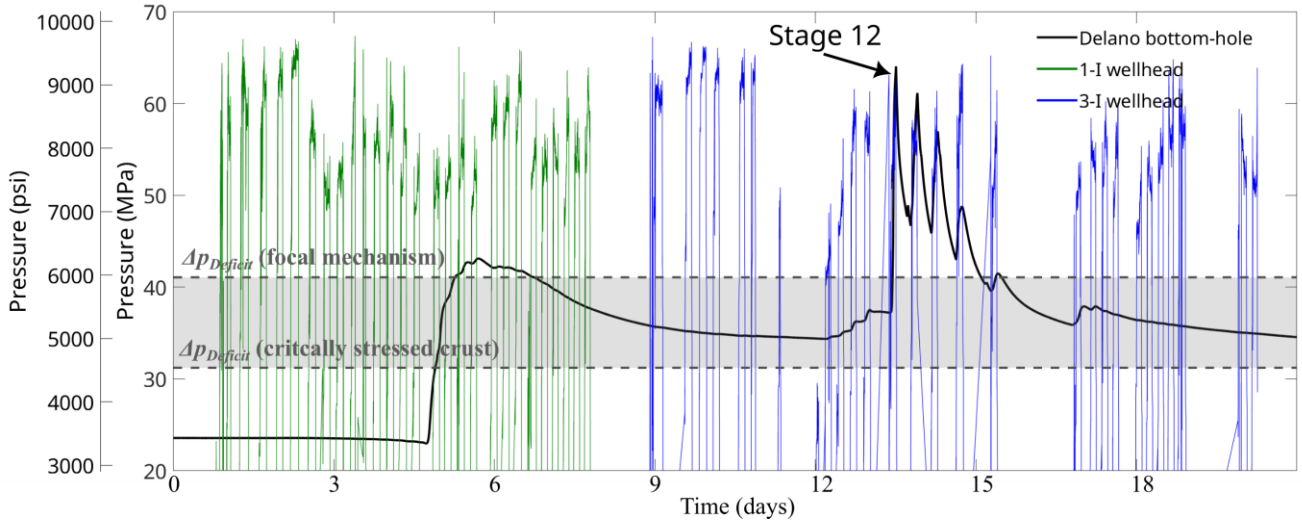

Figure 5: Downhole (black line) and wellhead pressures for 1-I (green lines) and 3-I (blue lines). The dashed horizontal lines and the shaded region in between indicate a realistic range of the pressure deficits from criticality on the fault under different assumptions for the maximum principal stress. The hydrostatic pressure difference between the wellhead and the Delano gauge is approximately 25 MPa. In addition, the wellhead pressures during stimulation are elevated due to frictional pressure drops from turbulent flow in the well and through perforations in the casing as well as flow through near-wellbore tortuosity.

3.1 Downhole Pressure Response due to Stimulation of 1-I

First, we examine the pressure increase that occurred during the 1-I stimulation. Figure 6 shows a map-view of the fault, the wells, and the hydraulic fractures that propagate along the angle of maximum horizontal stress from the center of each stage. Fig. 6 shows that hydraulic fractures from stage 13 pass close to the Delano gauge, provided that the half-length of the fractures is at least ~300 m. We hypothesize that leak-off from hydraulic fractures on the two sides of the gauge caused the first pressure increase shown in Fig. 5.

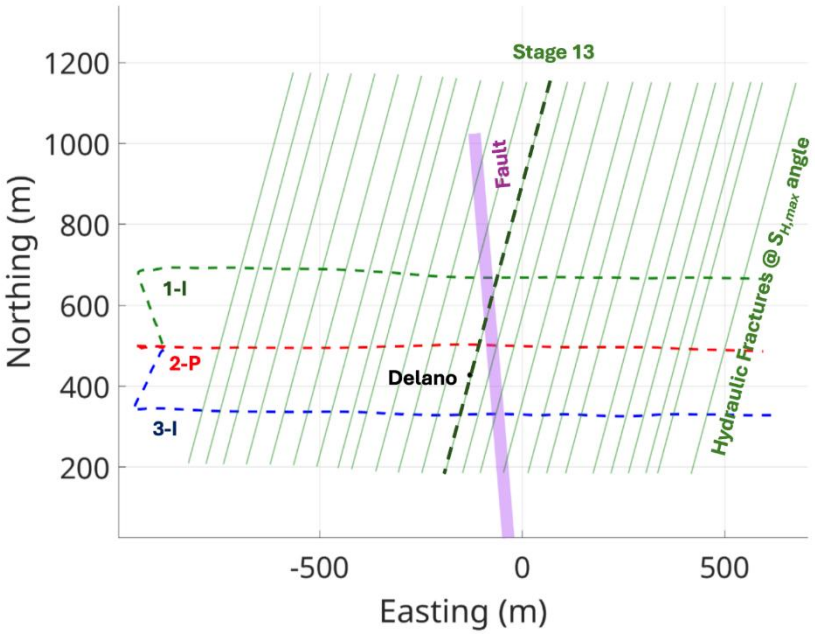

Figure 6: Map-view of the 1-I stimulation with respect to the fault (purple shaded line) and the Delano pressure gauge. The green lines represent hydraulic fracture that propagate from the centers of each stage along the angle of the maximum principal stress. Note that fractures from stage 13 would pass the closest to the Delano gauge, potentially developing multiple fractures that sandwich the Delano gauge in-between them (Figure 7a). The half-length of the fractures in the schematic is 500 m, but this value is poorly constrained and the actual length may be smaller. This will affect which stages produce hydraulic fractures that intersect the fault.

To test this hypothesis, we developed a 1D leak-off model that is similar to the Carter leak-off model (Howard & Fast, 1957) - which assumes constant fracture pressure and leak-off from a single fracture - but accounts for the geometry of parallel hydraulic fractures that propagate from multiple clusters and the depressurization from leak-off (Fig. 7a). The model also assumes 1D flow normal to the hydraulic fractures and neglects the longer timescale depressurization that comes from pressure diffusion beyond the finite height and length of the fractures. Balance of mass between the fluid inside the fracture and leak-off to the surrounding reservoir gives the following equations,

$$\beta_{res}\phi_{res}\frac{\partial p_{res}}{\partial t} = \frac{k}{\eta}\frac{\partial^2 p_{res}}{\partial x^2} \quad (1)$$

$$\beta_{HF}w_{HF}\frac{\partial p_{HF}}{\partial t} = 2\frac{k}{\eta}\frac{\partial p_{res}}{\partial x} \quad (1)$$

$$p_{HF}(t) = p_{res}(x = x_{HF},\, t) \quad (3)$$

$$p_{HF}(t=0) = p^{o}_{BHFP}\,,\; p_{res}(x,\, t=0) = p_{amb} \quad (4)$$

where p_{res} and p_{HF} are the pressures inside the reservoir and the hydraulic fractures, β_{res} is the sum of the pore and fluid compressibilities of the reservoir and β_{HF} is the compliance of the hydraulic fractures, φ_{res} is the porosity of the reservoir, k_{res} is the permeability of the reservoir, η is the fluid viscosity, and w_{HF} is the width of the hydraulic fracture. The boundary conditions of this problem are that there is pressure equilibrium at the fracture/reservoir interfaces (where $x = x_{HF}$) which are separated by the cluster spacing, L_{sep} (Figure 7a). The initial conditions are specified by equation (4), where the fracture pressure equals the estimated bottom hole fracture pressure, p^{o}_{BHFP}, and the reservoir pressure equals the ambient hydrostatic pressure, p_{amb}, of 25 MPa. This problem was solved analytically using Laplace transforms, with the inversion to the time domain performed numerically. The solution requires the hydraulic fracture compliance, which we estimated from fracture height estimates of approximately 200 m from low frequency DAS using fiber in the Delano well and elastic properties of the granite formation, and fluid transport properties like permeability obtained from toe stage diagnostic fracture injection tests (DFITs, also known as mini-fracs). The parameters of the model are summarized in Table 1. Results are shown in Fig. 7b which demonstrate that leak-off can explain the observed pressure change. This pressure increase is within the estimated range of the initial pressure deficit of the fault prior to stimulation (Figure 5). While the stimulation of 1-I may not have activated significant fault slip, it likely brought the fault to criticality prior to the subsequent stimulation of 3-I.

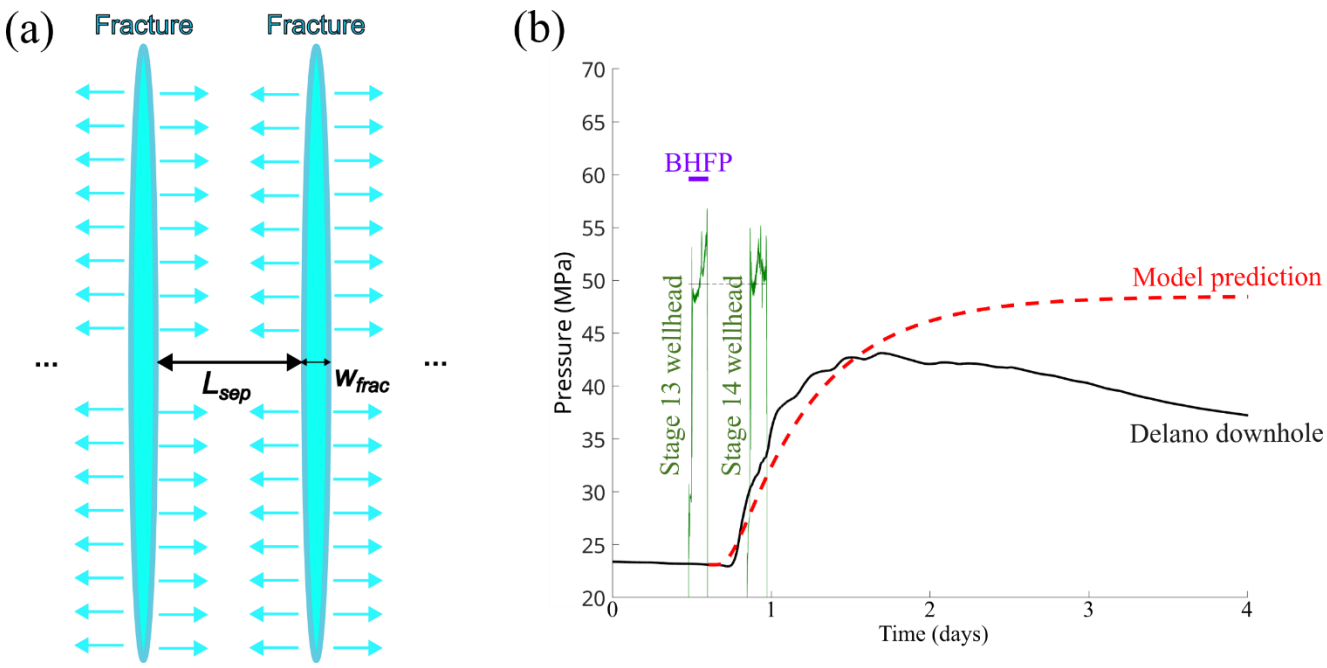

Figure 7: (a) Schematic of the parallel fracture, pressure-dependent leak-off model, outlined by equations (1) and (2). The model accounts for pressure-dependent leak-off that would occur during shut-in between parallel fractures that propagate from multiple clusters. (b) The model prediction (dashed red line) matches well the Delano pressure increase during the 1-I stimulation (black line). The green lines show the wellhead pressures during stimulation of stages 13 and 14. The purple line indicates the estimate of the bottom hole fracture pressure during stage 13 by the pumping company, which is used as the initial fracture pressure in the model. The parameters of the model are summarized in Table 1. Because the model assumes 1D flow and pressure diffusion normal to the hydraulic fracture, and neglects pressure diffusion into the 3D volume beyond the finite fracture height and length, it cannot explain the longer timescale depressurization seen in the data beyond day 2.

Table 8: Parameters of the leak-off models demonstrated in Figures 7 & 8.

Quantity	Value (units)
Stage 13 bottom hole fracture pressure (initial pressure inside hydraulic fractures)	59.8 (MPa)
Fracture height	200 (m)
Cluster spacing, L_{sep}	6 (m)
Fracture width, w_{HF}	1 (mm)
Reservoir permeability, k_{res}	2.274e-17 (m^2)
Dynamic viscosity, η	0.89e-3 (Pa s)
Fracture compressibility, β_{HF}	6.87e-6 (1/Pa)
Reservoir specific storage, $\beta_{res}\,\varphi$	5e-10 (1/Pa)

3.2 Downhole Pressure Response due to Stimulation of 3-I

Next, we examined the multiple spikes measured by the Delano gauge during the 3-I stimulation (Figure 5). The pressure history is notably different from the increase seen during 1-I stimulation, which occurred gradually over timescales longer than a single stage duration of a few hours. On the contrary, the pressure increase during the 3-I stimulation is comprised of six distinct pressure increases, characterized by a very rapid onset and more gradual (but still rapid compared to 1-I) decay. First, we tested the leak-off model that successfully explained the pressure increase during the 1-I stimulation. Figure 8a shows a map-view of the positions of the fault, the wells, and hydraulic fractures that propagate in the maximum horizontal stress direction from the center of each stage. Leak-off from stages 14 & 15, which

propagate fractures that run closest to the Delano gauge, cannot predict the rapid increase in pressure (Figure 8b). Furthermore, the largest pressure increase is observed during stimulation of stage 12 (Figure 8b), which is further away from the Delano gauge than stages 14 & 15 (Figure 8a). When modeling the pressure transmission to the Delano gauge through leak-off from stage 12 using a Carter leak-off model, the predicted pressure increase is negligible (Figure 8b). This conclusion holds even when accounting for uncertainty in the fault and hydraulic fracture orientations. We ultimately reject the hypothesis that the large pressure increases at Delano during the 3-I stimulation are due to leak-off from hydraulic fractures.

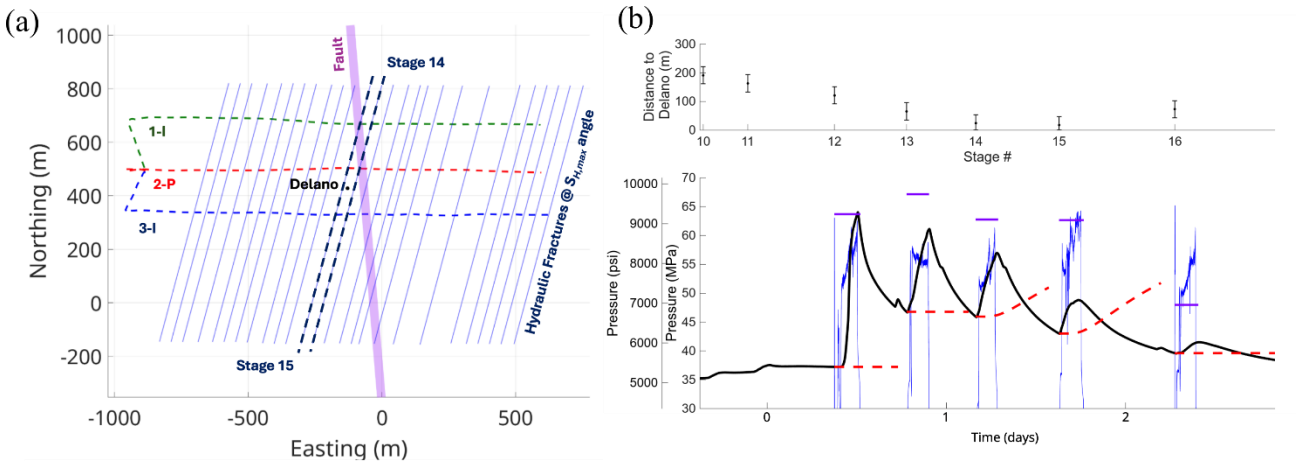

Figure 9: (a) Map-view of the 3-I stimulation with respect to the fault (purple shaded line) and the Delano pressure gauge. The solid blue lines represent hydraulic fractures that propagate from the centers of each stage in the direction of the maximum principal stress. The half-length of the fractures is drawn as 500 m, but this is poorly constrained and the fractures could be much shorter. (b) Bottom row shows comparisons between the predictions of the Delano pressure gauge by leak-off models (dashed red lines, calculated starting from the observed pressure at the start of each stage) to the data (black line). The top row shows the stage number and the fracture-normal distances to the Delano gauge; the latter are reported as a bar to acknowledge the finite length of the stage that contains multiple perforation clusters. Despite the proximity of stages 14 & 15 (dotted blue lines in (a)) to the Delano gauge, leak-off from these stages cannot match the rapid increase in pressure at the Delano gauge. Furthermore, the largest pressure increase is seen during stimulation of stage 12, which is another ~100 m further away from Delano with negligible leak-off contributions. Solid purple lines in (b) represent the bottom hole fracture pressure for each stage estimated by the pumping company.

An alternative hypothesis is that hydraulic fractures from 3-I intersect the fault. A schematic of this hypothesis is shown in Fig. 9. High pressure fluid is injected into the fault via the fractures and pressure is transmitted over 100 m along the fault zone to the Delano gauge (Figure 9), which is plausibly within the fault damage zone given uncertainty in the fault plane fit to the microseismic data (especially around the Delano gauge, where there are few microseismic events as shown in Figure 4). We believe that the multiple pressure spikes seen in the pressure data are created whenever hydraulic fractures intersect the fault zone, delivering additional high pressure fluid to the fault zone and transmitting pressure increases to the pressure gauge.

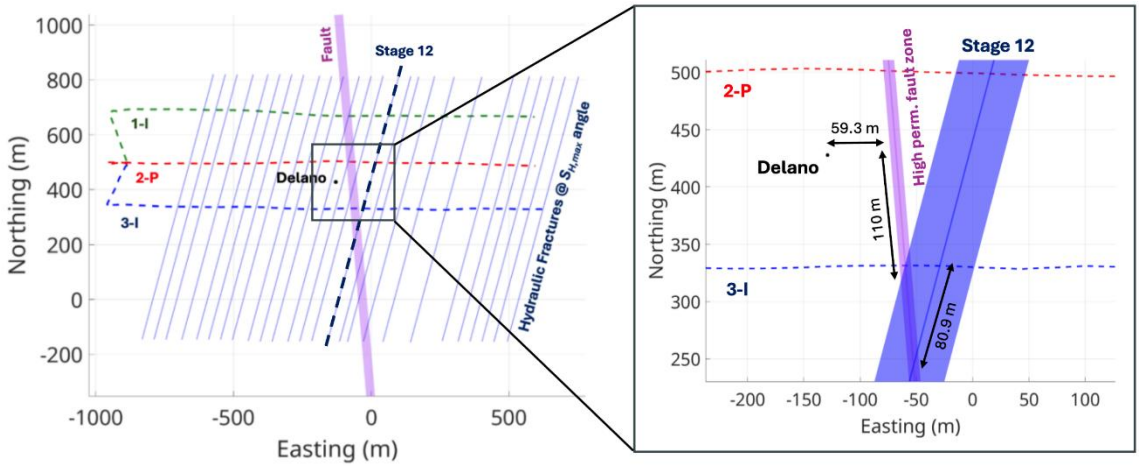

Figure 10: Map-view schematic of the fault-zone pressure transmission hypothesis. The solid blue lines represent hydraulic fractures that propagate from the centers of each stage in the direction of the maximum principal stress. The half-length of the fractures is drawn as 500 m, but this is poorly constrained. The fractures could be shorter, in which case fewer of them would intersect the fault. The shaded purple line represents the fault zone. The dotted blue line highlights hydraulic

fractures from stage 12 that make direct connections to the fault zone. The zoom-in inset shows that multiple clusters from stage 12 may drive hydraulic fractures along a relatively short distance (< 80 m) to the fault zone. The fault zone transmits pressure along a distance of approximately 100 m to the Delano gauge.

To quantitatively test this alternative hypothesis, we develop a pressure diffusion model along the fault zone that is directly connected to hydraulic fractures that propagate from the perforation clusters along the well. The model solves the 2D diffusion equation with constant permeability and time-dependent internal boundary conditions along intersections between the fault zone and hydraulic fractures. The internal boundary conditions enforce the estimated bottom hole fracture pressure during the stimulation of each stage at the fault/fracture intersections (Table 2). The model assumes fracture half-lengths of 500 m and heights of 200 m for single fractures that propagate from the center of each stage. The fault was initialized with stress and pressure conditions close to failure, as a consequence of the ~20 MPa pressure increase caused by the previous 1-I stimulation. Preliminary results from the fault zone diffusion model are shown in Figure 10. We prescribe a fault zone permeability of 5e-13 m^2, which is orders of magnitude higher than the permeability of the reservoir, 2.27e-17 m^2 that was estimated from toe stage DFITs. The high permeability of the fault zone leads to better matching of the high pressure increase observed at Delano (Figure 10d). This model demonstrates support for strong interactions between the hydraulic fractures and pre-existing fault zones in the reservoir at Cape Station such that the fault significantly influences the flow pattern during stimulation.

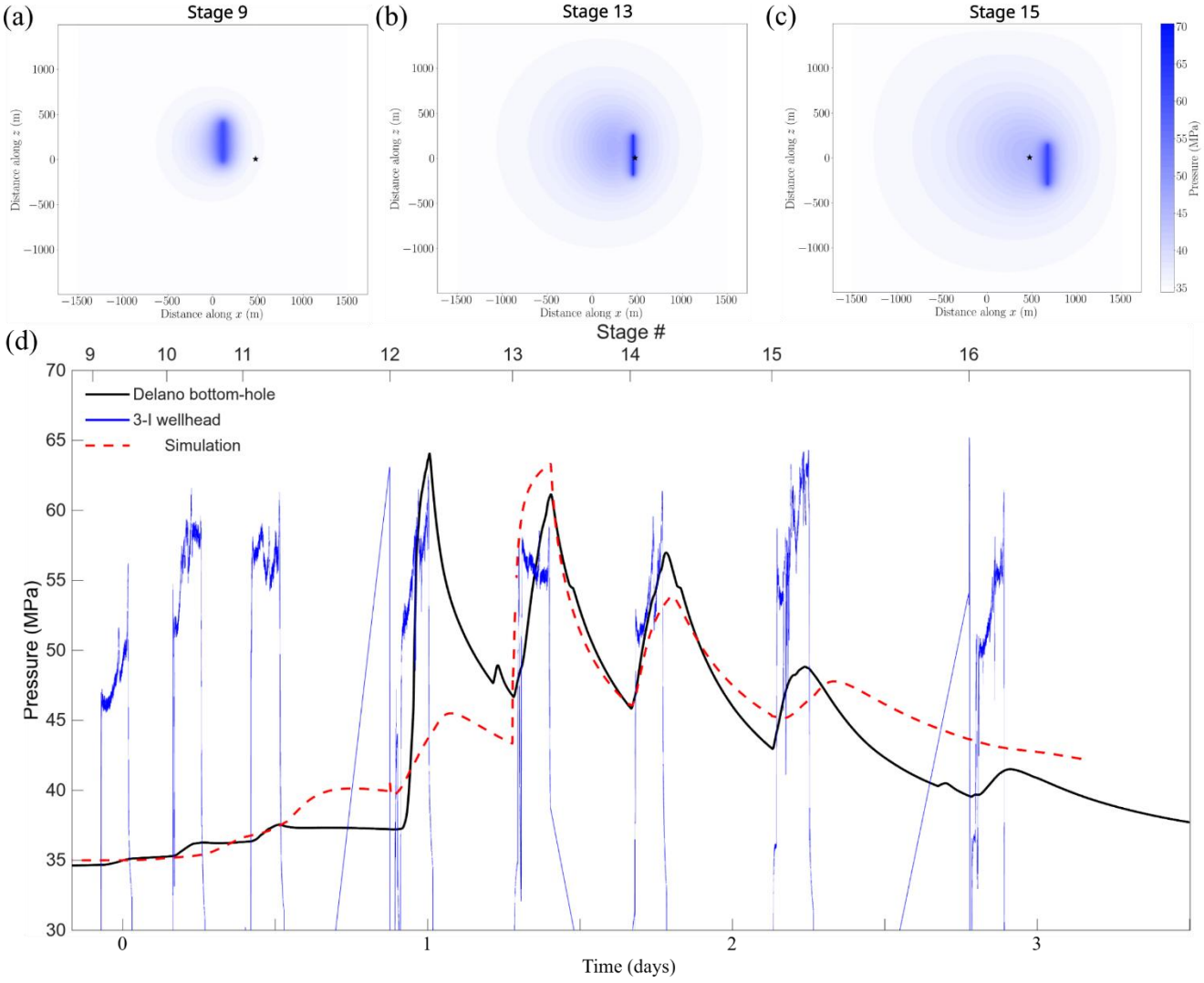

Figure 11: Fault zone pressure diffusion model connected to hydraulic fractures. (a)-(c) Contour plots of pressure along the 2-D fault zone show the evolution of pressure as internal boundary conditions enforce high pressures from the hydraulic fractures where the fractures intersect the fault. The black star indicates the projected location of the Delano gauge along the fault. (d) The fault zone model does a better job than the leak-off model (Figure 8b) in reproducing the high pressure increases at Delano. The parameters of the model are summarized in Table 2.

Table 12: Parameters of the fault zone diffusion model demonstrated in Figure 10.

Quantity	Value (units)
Bottom hole fracture pressure – used as fault zone fluid source pressure (for stages 9/10/11/12/13/14/15/16)	56.6/62.6/66.5/63.7/67.1/62.8/62.7/48.0 (MPa)
Fracture height	200 (m)
Fracture half-length	500 (m)
Fault zone permeability	5e-13 (m^2)
Dynamic viscosity	0.89e-3 (Pa s)
Fault zone specific storage	5e-10 (1/Pa)

The high bottom hole fracture pressures from the stages that intersect the fault (Table 2) imply high net pressure (~10 MPa) for minimum principal stress gradients estimated by injection tests (~0.85 psi/ft). Net pressures significantly higher than 1 MPa would produce unrealistically small fractures given the injected volumes. Possible explanations include stress-shadowing effects from stimulation of previous stages where fracture opening compresses the surrounding medium. However, it is unlikely that this would be enough to increase the minimum principal stress by ~10 MPa if the net pressure in all fractures is close to 1 MPa. Hydraulic fractures that terminate at faults could cause the pressure to increase to the necessary level to induce slip on the fault, if the fault only acquires significant permeability upon slipping. This could be significantly higher than the minimum principal stress, depending on the orientation of the fault. Another explanation is that hydraulic fractures grow along a series of small-scale natural fractures deviated from the angle of maximum principal stress, such that they are opening against a compressive stress greater than the minimum principal stress.

Parts of the model still show mismatch to the data. In particular, the model overestimates the pressure response from stage 11 while underestimating the pressure response from stage 12. The model neglects a number of important physical mechanisms such as the evolution of the fault zone permeability with slip. Additionally, we assume the growth of hydraulic fractures to be instantaneous. The length and the growth rate of the hydraulic fractures heavily influence the model results as it determines which stages make direct connections to the fault at what time. The model also simplifies the interactions between the hydraulic fractures and the fault zone at shut-in by neglecting the continued transfer of fluid from the fracture into the fault before closure. Future efforts will focus on accounting for these physical processes in more sophisticated models.

3. CONCLUSIONS

In this study, we examined the response and properties of a fault zone that was activated during multi-stage, plug-n-perf hydraulic stimulation of the wells from the Frisco pad at Cape Station, Utah, by Fervo Energy. We identify the fault that most likely caused minor casing deformation along one of the wells through unsupervised clustering of the microseismic catalog. The lack of seismic slip on this fault close the wells suggests that the casing deformation was caused by aseismic slip, undetected by the seismic monitoring. We model strong pressure signals at a downhole pressure gauge using a fault-zone pressure diffusion model, which supports the hypothesis that the same fault also facilitated the transmission of high pressure from hydraulic fractures to the pressure gauge. This pressure signal has features that differ from an earlier pressure increase at the downhole gauge which is sufficiently explained with leak-off from nearby hydraulic fractures. The earlier pressure increase likely brought the fault to criticality prior to the activation of microseismicity and the aseismic slip that caused casing deformation. The results demonstrate that strong interactions between hydraulic fractures and pre-existing faults can alter the flow paths in the reservoir and impact operations in enhanced geothermal systems. The analysis also shows the value of physics-based modeling, integrated with geophysical and geomechanical data, in managing EGS stimulation of faulted reservoirs.

ACKNOWLEDGEMENTS

This work was supported by the U.S. DOE under grant DE-EE0007080 “Enhanced Geothermal System Concept Testing and Development at the Milford City, Utah FORGE Site” and the Stanford Center for Induced and Triggered Seismicity (SCITS). Disclosure: Eric Dunham is a paid consultant to Seismos, Inc., a company that provides measurements to Fervo Energy. Those measurements were not used in this study.

REFERENCES

Cappa, F., Guglielmi, Y., & De Barros, L. (2022). Transient evolution of permeability and friction in a slowly slipping fault activated by fluid pressurization. *Nature communications*, *13*(1), 3039.

Cappa, F., Guglielmi, Y., Nussbaum, C., De Barros, L., & Birkholzer, J. (2022). Fluid migration in low-permeability faults driven by decoupling of fault slip and opening. *Nature Geoscience*, *15*(9), 747-751.

Fercho, S., Matson, G., McConville, E., Rhodes, G., Jordan, R., & Norbeck, J. (2024, February). Geology, temperature, geophysics, stress orientations, and natural fracturing in the Milford Valley, UT informed by the drilling results of the first horizontal wells at the Cape Modern Geothermal Project. In *Proceedings, 49th Stanford Workshop on Geothermal Reservoir Engineering*.

Fercho, S., Norbeck, J., Dadi, S., Matson, G., Borell, J., McConville, E., & Rhodes, G. (2025). Update on the Geology, Temperature, Fracturing, and Resource Potential at the Cape Geothermal Project Informed by Data Acquired from the Drilling of Additional Horizontal EGS Wells. In *Proceedings, 50th Workshop on Geothermal Reservoir Engineering* (pp. 1-13). Stanford University.

Häring, M. O., Schanz, U., Ladner, F., & Dyer, B. C. (2008). Characterisation of the Basel 1 enhanced geothermal system. Geothermics, 37(5), 469-495.

Howard, G. C., & Fast, C. R. (1957, January). Optimum fluid characteristics for fracture extension. In Drilling and production practice. OnePetro.

Guglielmi, Y., Cappa, F., Avouac, J. P., Henry, P., & Elsworth, D. (2015). Seismicity triggered by fluid injection–induced aseismic slip. *Science*, *348*(6240), 1224-1226.Kim, K. H., Ree, J. H., Kim, Y., Kim, S., Kang, S. Y., & Seo, W. (2018). Assessing whether the 2017 Mw 5.4 Pohang earthquake in South Korea was an induced event. *Science*, *360*(6392), 1007-1009.

Mohammadi, A., Chen, X., Nakata, N., & Dadi, S. (2025). Focal Mechanism and Stress Analysis of the CAPE Site, Utah. In *Proceedings, 50th Workshop on Geothermal Reservoir Engineering* (pp. 1-13). Stanford University.